Phase Fluctuations on the Micron-Submicron Scale in GUVs Composed of a Binary Lipid Mixture

Anna Celli, Sabrina Beretta, and Enrico Gratton
Laboratory for Fluorescence Dynamics, Department of Biomedical Engineering, University of California at Irvine, Irvine, California

ABSTRACT We used a combination of imaging and fluctuation techniques to investigate the temporal evolution of gel phase domains at the onset of phase separation, as well as the correlation between domain topology and local lipid ordering in GUVs composed of a binary mixture of DPPC/DLPC 1:1. The data acquired at temperatures immediately above the transition temperature of the two lipids suggest fluctuations in the lipid organization with a lifetime <0.1 s and a characteristic length of 1.2 μm. As the temperature is decreased below the transition temperature of one of the lipids, coupling between the two leaflets of the bilayer is observed to begin within the first five minutes after the onset of phase separation. However, domains confined to only one leaflet can be found during the first 45–50 min after the onset of phase separation. Our analysis using a two-state model (liquid and gel) indicates that for the first 45–50 min from the onset of phase separation the two lipid phases do not strongly influence the phase behavior of each other on the micron-length scale. At longer times, behavior that deviates from the two-state model is observed and appears to be correlated to domain morphology.

INTRODUCTION

Fluctuations in lipid membrane organization have been the object of an ever growing number of theoretical and experimental studies because they are fundamental to the understanding of basic principles governing the complex structural and functional organization of biological membranes.

The main interest in lipid membranes arises from its biological relevance, since lipids form the structural matrix of the cell membrane. It is now established that lipid molecules do not play only a structural role in the membrane. In particular, fluctuations in the lipid organization (such as those associated with membrane rafts; see (1) for a review) appear to be crucial to many cellular functions (2); from protein polymerization, to liposome budding and viral infection (3,4).

In cell membranes, experimental evidence suggests the existence of submicron-scale rafts (4–7). Due to the small dimension and transient nature of such lipid domains in cell membranes, the use of experimental techniques with high temporal and spatial resolution is necessary for their study.

Despite the extensive work on lipid phase behavior, a clear understanding of the mechanisms regulating the formation and the dynamics of lipid organizational fluctuations is still lacking even for much simpler systems such as model bilayers. Direct evidence of lipid phase separation in model lipid membranes has been obtained by a number of experimental techniques. Among these, NMR (8,9) and atomic force microscopy (10,11), have shown the presence of submicron-sized phase domains below the miscibility transition in phosphocholine mixtures. Fluorescence microscopy has allowed the direct visualization and morphological characterization of micron-size domains on freestanding bilayers for a wide number of lipid mixtures (12–18). Lipid domain formation and morphology has also been modeled computationally especially with regard to the study of obstructed diffusion and membrane curvature (19–21).

Another problem related to lipid domain formation and morphology is that of leaflet coupling, i.e. whether the domains are confined to only one leaflet or span the bilayer. In cell membranes, several studies suggest coupling between rafts in the inner and outer leaflets (6,7,22), despite the difference in chemical composition of the two leaflets (23). Studies on supported, chemically asymmetric bilayers suggest that lipid phase domains can induce ordering in the opposite leaflet (24). In freestanding bilayers, the two opposing leaflets have the same chemical composition. Leaflet coupling in freestanding model bilayers displaying phase separation has been reported for a variety of lipid mixtures including phosphocholine binary mixtures (12,15,25,26). Little investigation has been done, however, on the mechanisms and dynamics of leaflet coupling.

The experiments presented in this article were carried out with the purpose of investigating the dynamics of submicron and micron domain formation in model membranes composed of two lipids with different transition temperatures. The objective is to follow their organizational and morphological development over time, focusing, in particular, on the orientation of the lipid molecules, the level of coupling between the leaflets, and the interaction of the two phases with each other. By interaction between the two lipid phases, we mean the deviation from a noninteracting two phase state (gel and liquid-crystalline) model of the binary mixture. Previous time-resolved fluorescence studies on

Submitted January 26, 2007, and accepted for publication August 6, 2007.

Address reprint requests to Anna Celli, Tel.: 217-721-1310; E-mail: celli.anna@gmail.com.

Anna Celli's present address is VAMC, 4150 Clement St., San Francisco, CA, 94121-1545.

Editor: Lukas K. Tamm.

0006-3495/08/01/104/13 $2.00

doi: 10.1529/biophysj.107.105353

phosphocholine binary mixtures have provided indirect evidence for deviation from a two-state system (27).

Lipid freestanding bilayers were reconstituted in giant unilamellar vesicles (GUVs). The geometry and size (similar to that of a cell) of GUVs allows direct visualization of the membrane under the microscope (14,28). The use of freestanding bilayers also eliminates possible artifacts due to contact with the substrate (29). A 1,2-Dipalmitoyl-3-*sn*-glycero-phosphocholine (DPPC), 1,2-dilauroy-3-*sn*-glycero-phosphocholine (DLPC) in a 1:1 mixture was used for our experiments. This mixture is well characterized and it is known to display phase separation between liquid-crystalline and gel in a wide temperature range. The small mismatch between the acyl chains of the two lipid species (four carbons) results in low line tension between the fluid and gel phases (25,30,31). By keeping the sample at a temperature close to that of the DPPC main phase transition (41.2°C), we were able to visualize the formation of micron-size gel domains and follow their spatiotemporal evolution.

Our approach to the study of domain formation is based on the use of the fluorescent properties of the environment-sensitive dye Laurdan. In lipid membranes, Laurdan's emission spectrum maximum performs a red shift from 440 nm (I_{440}) in the gel phase to 490 nm (I_{490}) in the liquid-crystalline phase. Laurdan has been employed in many studies on lipid phase behavior due to the sensitivity of its emission spectrum to the local packing of the lipids on the membrane (13,14,27,28,32–37) which reports on the local lipid density. The dye spectral shift (and therefore the lipid phase) can be quantified using the generalized polarization function (GP) introduced by Parasassi and Gratton (34). In addition to the spectral behavior, the orientation of Laurdan's excitation dipole parallel to the lipids' acyl chains reports on the level of ordering and on the alignment (with respect to the plane of the membrane) of the acyl chains. Another important feature of Laurdan is that it partitions equally in the liquid-crystalline and gel phases (27,36). This property constitutes an advantage over partitioning dyes in the study of lipid phase fluctuations. In fact, while partitioning dyes give an on-/off-response to the presence of domains, the sensitivity of Laurdan to the lipid environment allows the investigation of intermediate stages of domain formation.

Two-photon excitation microscopy has allowed the use of Laurdan in microscopy studies on lipid membranes due to the low photo toxicity of this technique and the capability of using 700 nm light to excite in the UV region (350 nm) using glass objectives. In our setup, two channels in the emission collect the fluorescence at 440 nm and 490 nm.

Two modes of data acquisition were used: raster scanning images and circular scanning. In the latter, the laser beam is scanned in a circular orbit over the sample allowing higher temporal resolution. GP autocorrelation curves were calculated from the circular scanning data to qualitatively follow the average size and number of phase fluctuations (diffusion motility).

To establish whether the forming domains are homogeneous in their phase composition, and to estimate the deviation of the system from a noninteracting, pure two-state model, we developed a data analysis method that allows estimation of the fractional percentage of lipid molecules in the gel phase for each data point.

We found a wide spatial heterogeneity in the membrane organization at different times after the onset of phase separation. In particular, we observe micron-sized areas with 40–50% gel fraction that we attribute to domains in which the leaflet coupling is incomplete.

MATERIALS AND METHODS

Materials

1,2-Dipalmitoyl-3-*sn*-glycero-phosphocholine (DPPC) and 1,2-dilauroy-3-*sn*-glycerophosphocholine (DLPC) dissolved in chloroform were purchased from Avanti Polar Lipids (Alabaster, AL). Laurdan in powder was purchased from Molecular Probes (Eugene, OR).

Experimental setup

Two-photon fluorescence microscopy

We used a home-built two-photon excitation microscope for the measurements described in this article. Two-photon excitation is a nonlinear process in which the fluorophore excitation occurs by the simultaneous absorption of two photons. The high photon density required for the process limits the excitation to the focal plane, thus providing high spatial resolution on the z axes and low out-of-focus photodamage.

Our custom made two-photon system was built around the body of a Axiovert microscope (Carl Zeiss, Jena, Germany) and was previously described by Bagatolli and Gratton (13). An optically pumped (Verdi, Coherent, Santa Clara, CA) tunable mode-locked Titanium-Sapphire laser (model No. 900, Mira, Coherent) provides high peak, power-pulsed excitation light. The pulse frequency is 80 MHz and the excitation wavelength used was 780 nm. A quarter-wave plate was used to circularly polarize the excitation light. We used neutral density filters before the microscope to reduce the average laser power before entering the microscope power to 70 mW. The estimated power at the sample is ~10 mW. The beam is scanned at the back port of the microscope by a set of galvanometric mirrors. A dichroic mirror reflects the excitation light into a 0.4 N.A. 20× objective (LD Achroplan R, Carl Zeiss). The lateral dimension of the point spread function (PSF) of the system was measured to be 0.7 μm. The emitted fluorescence light is collected by the same objective and transmitted by the dichroic. Another dichroic in the emission path splits the fluorescence by reflecting light with a wavelength <470 nm and transmitting the rest. The reflected light passes through a band pass filter with a width of 46 nm and centered at 446 nm and is detected by the blue PMT. Another broad band pass filter with the same width and centered at 499 nm is placed in the path of the transmitted light in front of the green PMT. The data from the two channels are collected and stored in a PC. We refer to the intensity collected in the two channels as I_B and I_G for the blue and green PMTs, respectively. The data acquisition/analysis program SimFCS (http://www.lfd.uci.edu/globals/) controls the motion of the mirrors and the integration time of each data point in addition to processing and analyzing the data in real time.

Sample preparation

GUVs were prepared following the electroformation method described by Angelova (38), 3 μl of a 0.2 mg/ml solution of lipids in chloroform were

spread on each of two platinum electrodes of the electroformation chamber previously described by Bagatolli (39). The excess chloroform is removed by placing the chamber for 1 h in a lyophilizer or under an N_2 stream. The bottom of the chamber is then sealed, the chamber is secured on the microscope, then connected to a heat bath at a temperature of 50°C and 4 ml of nanopure water at the same temperature is added to the chamber. The electrodes are connected to an alternating current field with an amplitude of 3 mV and a frequency of 10 Hz. After 40 min, 2 μl of a 0.2 mM solution of Laurdan in DMSO is added to the buffer. The field is switched off after 15 additional minutes. The temperature is then decreased at a rate of 1°C every 10 min and finally kept constant at 40 ± 1°C.

Methods

Laurdan

Specifically designed by Gregorio Weber (40,41) as a solvent dipolar relaxation sensitive dye, Laurdan has proven to be an excellent tool for the investigation of lipid phase behavior thanks to the sensitivity of its emission and excitation spectra to the level of water penetration in the membrane (42–45). The 12 carbon acyl chain of Laurdan anchors the dye to the lipid membrane in such a way that its fluorescent moiety is in contact with the glycerol backbone of the lipids. When the lipids are in the gel ordered phase, the Laurdan emission spectra is centered at 440 nm. When the lipids are in the liquid-crystalline, disordered phase, water molecules can penetrate down to the lipid glycerol group causing the emission spectra to relax and the emission spectra center of mass red shifts to 490 nm. The dye dipolar relaxation occurs during the life time of the dye excited state. The lipid phase-sensitive shift in the Laurdan emission spectra can be quantified by the use of the GP function which was first introduced by Parasassi and Gratton (27). The GP is defined as

$$GP = \frac{I_B - I_G}{I_B + I_G}, \quad (1)$$

where I_B and I_G are the fluorescence intensity collected at 423–469 nm (blue channel) and at 476–522 nm (green channel), respectively. High values of GP indicate that the membrane is in the lipid gel phase, while the lipid liquid-crystalline phase is characterized by low GP values.

Another useful characteristic of the dye Laurdan in the visualization of lipid phase domains is the photo-selection effect (Fig. 1) which arises from the position of the dye molecule in the bilayer. The excitation dipole of the fluorescent moiety of Laurdan is aligned parallel to the lipid acyl chains. When the lipids are in the liquid-crystalline disordered phase, the disorder in the acyl chains allows the Laurdan excitation dipole to tilt off axes, while in the lipid gel-ordered phase, the excitation dipole is more rigidly aligned orthogonally to the surface of the lipid membrane. On the polar region of GUVs, as defined in Fig. 1, when Laurdan is in the lipid gel phase, its excitation dipole is orthogonal to the plane of polarization of the light and therefore no excitation can occur. In the liquid-crystalline phase, however, the disorder in the acyl chains allows the Laurdan excitation dipole to tilt off axes. Excitation can therefore occur. As a consequence, gel domains appear as dark areas on the polar region of the membrane.

In the GUV polar regions, therefore, a gel domain is expected to be characterized by both a high (positive) GP value, due to the spectral effect, and a low fluorescence intensity in both channels, due to the photo-selection effect. Notice, however, that these two properties of the dye Laurdan give information on two different aspects of the lipid organization in the bilayer. The spectral effect, by reporting on the level of water penetration in the membrane, gives information on the packing density of the lipids, while the photo-selection effect reports on the radial alignment of the lipids. All of the experiments presented here were performed on the polar region of the vesicles.

Data acquisition

Two data acquisition modes were used: imaging and circular scanning. In the former, two voltage ramps are applied to the galvanometric mirrors and the excitation beam is raster-scanned across the sample. The typical acquisition time for one frame is 6 s. In the circular scanning mode, two sinusoidal voltages are applied to the mirrors and the beam is scanned across the sample in a circular orbit. Circular scanning measurements allow higher temporal resolution (up to three orders-of-magnitude faster timescales) while still providing some spatial information. Moreover, the fact that the excitation volume is scanned on the sample reduces photobleaching when compared with single point fluctuation experiments. The center, radius of the orbit (r_o), period of scanning, and the acquisition frequency are set in the acquisition program by the user. For the data presented below, we used a period of scanning of 0.1 s and an acquisition time of 100 μs. Faster scanning periods (up to 2 ms) did not yield further information. The number of data points per orbit (n_p) is determined by the product of the period of scanning and the acquisition frequency. The distance between two adjacent points in one orbit (d_p) is determined by the ratio between the orbit circumference and n_p. In the data presented below, d_p is on the order of 20–40 nm, much smaller than the PSF to guarantee a homogeneous sampling of the scanned region. The values of d_p and n_p are specified in the legend of each image.

The GP is calculated in the same way for both imaging and circular scanning data. The difference between the intensity in the two channels

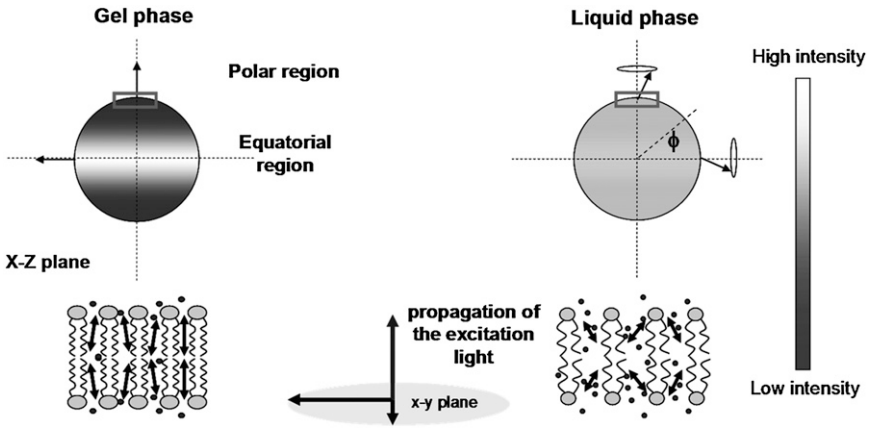

FIGURE 1 Location of Laurdan in the membrane and photoselection effect. The location of Laurdan excitation dipole (represented as *arrows*) in the lipid bilayer is schematically shown in the bottom part of the image. The Laurdan excitation dipole is highly aligned orthogonal to the membrane surface when the lipids are in the gel phase. In the liquid-crystalline phase the Laurdan excitation dipole is freer to tilt off axes due to the higher disorder in the lipid acyl chains. The top part of the image shows the effects of the different alignments of Laurdan when imaging GUVs: in the gel phase, the dye molecules on the polar region of the vesicle are not excited as their dipole moment is orthogonal to the plane of polarization of the light. In the liquid-crystalline phase we have a component of the excitation dipole parallel to the plane of light polarization and the dye can therefore be excited. Note that the polar and equatorial regions of the GUV are defined with respect to the direction of light propagation.

measured at each data point is calculated and normalized to the total intensity collected at that data point.

The circular scanning data can be visualized in pseudo-images in which each horizontal line represents the scanned orbit at different times. Horizontal lines will therefore represent the spatial information, while vertical lines represent the time evolution of each point on the orbit. This type of data rendering allows easy visualization of lipid domains in both the intensity and the GP traces.

Data analysis: the two-state model curve

In the GP images, the GP value calculated at each pixel reports on the local phase state of the membrane. High and low GP values indicate that the lipids are in the tightly packed gel phase and disordered liquid crystalline phase, respectively. An intermediate GP value at a pixel can be explained either by a phase which is intermediate between pure liquid and pure gel, or by the coexistence of subdiffraction domains as discussed in the literature (36,37). In the case of the coexistence of noninteracting subdiffraction lipid domains (two-state model), we can calculate the functional dependence of the GP on the fluorescence intensity measured in each one of the two channels. We assume that the measured intensities in the blue (green) channel is given by the fraction of molecules in the gel phase, α, times the fluorescence intensity emitted in the blue (green) channel by those molecules plus the fraction of molecules in the liquid-crystalline phase, β, times the fluorescence intensity emitted in the blue (green) channel by those molecules:

$$I^{\mathrm{B}} = \alpha I^{\mathrm{B}}_{\mathrm{gel}} + \beta I^{\mathrm{B}}_{\mathrm{liquid}}$$
$$I^{\mathrm{G}} = \alpha I^{\mathrm{G}}_{\mathrm{gel}} + \beta I^{\mathrm{G}}_{\mathrm{liquid}}. \quad (2)$$

Assuming that only those two states exist (therefore $\alpha + \beta = 1$), we then have

$$\alpha = \frac{I^{\mathrm{G}} - I^{\mathrm{G}}_{\mathrm{l}}}{I^{\mathrm{G}}_{\mathrm{g}} - I^{\mathrm{G}}_{\mathrm{l}}}. \quad (3)$$

Substituting the expression for α, I^{B}, and I^{G} into Eq. 1, we find an expression for the GP as a function of the intensity in the two channels:

$$GP = \frac{I^{\mathrm{G}}(I^{\mathrm{B}}_{\mathrm{g}} - I^{\mathrm{B}}_{\mathrm{l}} - I^{\mathrm{G}}_{\mathrm{g}} + I^{\mathrm{G}}_{\mathrm{l}}) - (I^{\mathrm{G}}_{\mathrm{l}} I^{\mathrm{B}}_{\mathrm{g}} - I^{\mathrm{G}}_{\mathrm{g}} I^{\mathrm{B}}_{\mathrm{l}})}{I^{\mathrm{G}}(I^{\mathrm{B}}_{\mathrm{g}} - I^{\mathrm{B}}_{\mathrm{l}} + I^{\mathrm{G}}_{\mathrm{g}} - I^{\mathrm{G}}_{\mathrm{l}}) - (I^{\mathrm{G}}_{\mathrm{l}} I^{\mathrm{B}}_{\mathrm{g}} - I^{\mathrm{G}}_{\mathrm{g}} I^{\mathrm{B}}_{\mathrm{l}})}. \quad (4)$$

Notice that, in this case, $I^{\mathrm{B}}_{\mathrm{g/l}}$ and $I^{\mathrm{G}}_{\mathrm{g/l}}$ represent the intensity in the blue and green channel of a pixel in the pure gel and liquid phase, respectively. From the experimental data in the limiting conditions in which we have a pure gel phase and a pure liquid phase we estimate the values of $I^{\mathrm{B}}_{\mathrm{g/l}}$ and $I^{\mathrm{G}}_{\mathrm{g/l}}$. By inversion of Eq. 4 we can link a given pair of GP and I^{G} to the fraction of molecules in the gel phase. In our experimental conditions, the characteristic GP of a gel domain is found to be 0.27 ± 0.04, while the characteristic GP for the liquid phase at 41.0°C is found to be -0.34 ± 0.02.

Data analysis: two-dimensional (2D) histogram

To estimate the unknown parameters in Eq. 4, namely the fraction α of gel phase in a pixel and the values of $I^{\mathrm{B}}_{\mathrm{g/l}}$ and $I^{\mathrm{G}}_{\mathrm{g/l}}$, we construct a 2D histogram from the circular scanning data which represents how many points in the data set have a given value of GP and intensity in one of the two channels. This type of representation allows for the investigation of the relation between the packing of the lipids (as reported by the GP) and the level of alignment of the lipid (as reported by the fluorescence intensity in each channel which is related to the alignment of the Laurdan excitation dipole). In fact, if the lipids are perfectly aligned (Laurdan is aligned along the lipids) the fluorescence intensity (not the GP) will be low, because photo-selection forbids excitation of these molecules that are aligned perpendicular to the bilayer surface, when we illuminate the top or the bottom of the GUV.

The 2D histograms are obtained by dividing the intensity and the GP range (which can be selected by the user) in a user-defined number of bins (in the case of 256 intensity and GP bins we have 65,536 2D intervals). Then the data points with intensity and GP in the range of each of the two dimensional intervals are counted. The result is displayed in the 256×256 images in which a color scale indicates the frequency of occurrence at each 2D interval.

The 2D histograms are used to evaluate the unknown parameters in Eq. 4, thus allowing an estimate of the fraction of gel phase present at each pixel. Notice that the 2D histograms represent a 2D distribution of the data point in the GP/intensity space. The calculation of an analytical form for such a 2D distribution is not trivial since the individual one-dimensional GP and intensity distributions for each GP and intensity coordinate are not independent from each other. The determination of such an analytical expression goes beyond the scope of this article. A traditional least χ^2 fit of the form $y = f(x)$ is therefore not possible for our 2D histograms. Instead we developed a ''best score'' method which allows us to compare the experimental 2D distribution to the two-state approximation curve of Eq. 4. The parameters of Eq. 4 are entered in the data analysis program and the GP versus green (blue) intensity is calculated using Eq. 4. A score, determined by the number of points at a user-determined distance from the curve, is calculated by the data analysis program. The unknown parameters are manually varied until the best (highest) score is obtained. There are four unknown parameters in Eq. 4. However, they are linked by the condition that the GPs of the liquid and gel phases are equal to a specific value determined separately for the pure gel and the pure liquid samples.

Mapping of the two-dimensional (2D) histogram

We can map selected areas of the 2D histogram back into the pseudo-images. This allows us to study both the spatial and the temporal changes in the pseudo-pixel gel fraction. In the GP and intensity pseudo-images, the points in a given GP-intensity interval are highlighted (in *red* in Figs. 5, 8, and 9) as a cursor is moved on the 2D histogram. This type of analysis yields information on the spatial organization and temporal evolution of the domains.

Data analysis: GP-autocorrelation curves (GP-ACF)

To detect the presence of spatial and temporal correlation in the GP traces of the circular scanning data, we calculated the autocorrelation function of the GP signal defined as

$$GP - ACF(\tau) = \frac{\langle S(t)S(t+\tau)\rangle}{\langle S(t)\rangle^2} - 1, \quad (5)$$

where $S(t)$ is the GP signal at time t. In the case of circular scanning data, the autocorrelation function has the typical oscillating structure (46,47) where the decay of the periodic peaks indicates the temporal decay of the correlation while the shape of the peaks reflects the presence of structures in the scanned orbit. Therefore the GP-autocorrelation curve calculated from circular scanning data contains both spatial and temporal information. The mathematical basis for the separation of the temporal and spatial information is discussed in the literature (48,49). In the following, we use the GP-autocorrelation curves as a qualitative indicator of the self similarity of the GP signal. In particular, the initial amplitude of the autocorrelation curve ($G(0)$) is related inversely to the number of objects (lipid phase domains) fluctuating on the scanned orbit and is directly related to the contrast between the GP signal from the domains and the background. The shape (particularly the width) of the first decay of the curve yields information on the characteristic size of the structures in the scanned orbit.

RESULTS

Our experiments were all performed on GUVs made of a DPPC/DLPC 1:1 mixture. The GUVs were grown at 50°C

and the temperature was later decreased to the one required for each particular experiment. Data were acquired at temperature above the phase transition of both lipids and at the temperature where the system undergoes phase separation.

Data at temperatures just above the phase transition of both lipids

We collected both images and circular scanning data on the top surface of the vesicle before phase separation is observed. Fig. 2 shows the circular scanning data collected at 43.1°C (*top panel*) and 41.2°C (*bottom panel*). Fig. 2, *A* and *D*, show the circular scanning intensity and GP data rendered as pseudo-images. The 2D histograms at these temperatures are shown in Fig. 2, *B* and *E*, respectively, while Fig. 2, *C* and *F*, show the autocorrelation curves calculated from the GP traces. Both the GP images and pseudo-images appear homogeneous at both temperatures (Fig. 2, *A* and *D*).

At both temperatures, we notice the same behavior of the 2D distributions. From the GP-versus-I_{490} histograms (Fig. 2, *B* and *E*, *left histograms*), we notice that high green fluorescence intensity is associated with low GP values, while in the GP-versus-blue intensity histograms (Fig. 2, *B* and *E*, *right histograms*) we observe the opposite behavior (i.e., high blue intensity corresponds to high GP). The specific shape of these 2D histograms is a consequence of the spectral behavior of Laurdan and of the definition of GP. However, the correlation between high GP (which is an indicator of tight lipid packing) and high intensity in the blue channel implies that there is no strong preferential alignment of the Laurdan excitation dipole in the data points with a higher GP value at this temperature.

The GP-autocorrelation curves at the temperature above the phase separation were calculated to detect the presence of spatial and temporal correlation in the lipid organization before the phase separation. The curves are shown in Fig. 2, *C* and *F*. The curves show an increasing spatial and temporal correlation as the DPPC phase transition temperature is approached. The curve in Fig. 2 *C* shows the presence of correlation for at least 6 ms (corresponding to ~1.2 μm) at 43.1°C. At this temperature, the periodic oscillations of the curve decay after the first orbit, indicating the absence of stable structures. Closer to the phase separation temperature, at $T = 41.2$°C (Fig. 2 *F*), when no domains can be resolved by either the intensity or the GP, the curves decay with longer characteristic times indicating the presence of long-range correlation (on the order of 40 ms, which corresponds to 8 μm). At this temperature we also detect a slower decay of the periodic oscillations indicating that more stable structures are now present. It is important to point out that in the GP pseudo-images of the pre-phase-separation data (Fig. 2, *A* and *D*) no micron-size structures are visible.

Data at temperature of phase coexistence

Submicron-sized domains were generated by inducing phase separation in the binary mixture membrane. By keeping the sample at a temperature close to that of the DPPC main phase transition (41.2°C) we were able to visualize the formation of

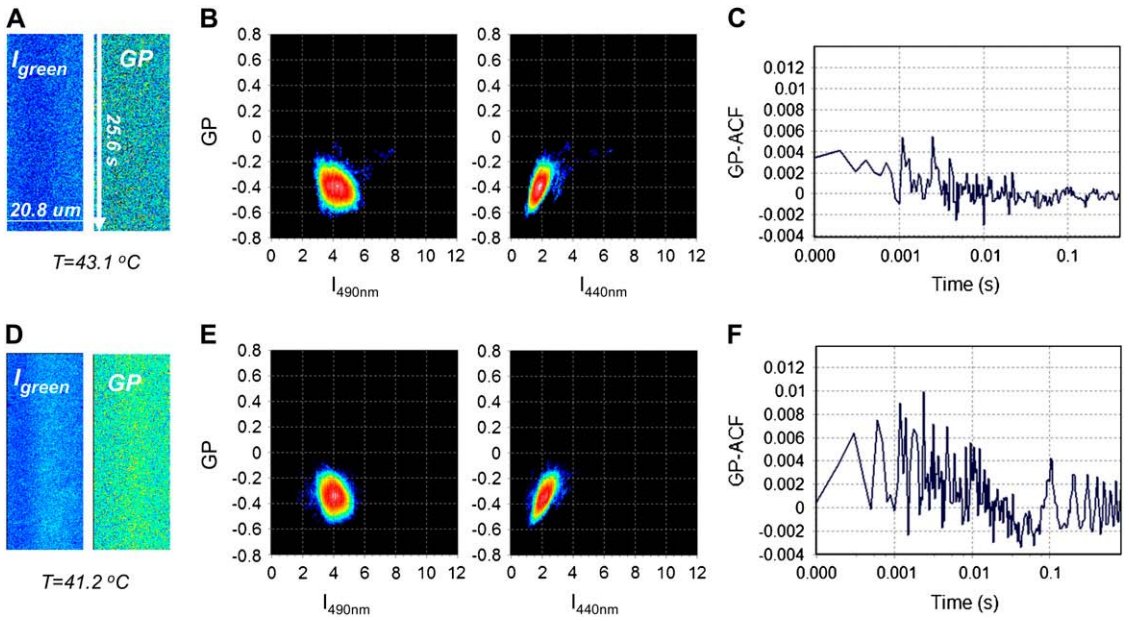

FIGURE 2 Circular scanning data above phase separation for DPPC/DLPC 1:1. (*Top panel*) $T = 43.1$°C. (*Bottom panel*) $T = 41.2$°C. (*A* and *D*) Pseudo-images of intensity in the green channel (*left*) and GP (*right*). (*B* and *E*) Two-dimensional histogram of GP versus intensity in the green channel, I_{490} (*left*) and 2D histogram of GP versus intensity in the blue channel, I_{440} (*right*). (*C* and *F*) GP autocorrelation curve. Each pseudo-image shows a 20.8-μm portion of the scanned trajectory in a 25.6 s time frame. For both panels *A* and *B*, $t_p = 0.1$s, $n_p = 1000$, and $d_p = 21$ nm.

micron-size gel domains and follow their spatiotemporal evolution.

Images

Fig. 3 shows the morphological evolution of the gel domains, as visualized by the raster-scanned fluorescence images. We observe phase separation for this mixture at ~40.6°C. The first domains observed move in directions uncorrelated with each other, have a circular shape with a diameter of ~3 μm (Fig. 3 *B*) and diffuse on the vesicle surface at an average speed of 0.7 μm/s. After ~5 min from the initial observation of round gel domains we observe larger circular domains (with an average diameter of 7–9 μm) which are clustered together (Fig. 3 *C*), in addition, to the smaller domains. After the domains reach the size of 7–9 μm, the circular symmetry is broken and spider weblike patterns are observed (Fig. 3 *D*). After >1 h at constant temperature, a combination of circular domains and lines branching out of them is observed (Fig. 3 *E*). As the temperature is further decreased (data not shown), thicker wire-shaped domains are observed in agreement with observations reported by Bagatolli (25).

In the images in Fig. 3, gel domains are dark, implying strong radial alignment of the dye molecules perpendicular to the bilayer surface. This observation implies high ordering of the lipid molecules and coupling between the two leaflets of the bilayer, as discussed by Bagatolli (25).

Circular scanning measurements

Circular scanning measurements were performed on vesicles close to the DPPC phase transition temperature, 41.2°C (n_p and d_p are specified in the legend for each pseudo-image). Fig. 4 (*top panel*) shows the circular scanning data at the onset of phase separation. Fig. 4 *B* shows in detail the intensities of both channels and the GP trace at the position of the dashed red line in Fig. 2 *A*. These measurements allowed us to detect micron-sized lipid domains at 41.0 ± 0.5°C, as can be seen in the green channel intensity (I_{490}) pseudo-images in Fig. 4 *A* (*left*). Surprisingly, the GP pseudo-image (Fig. 4 *A*, *right*) looks homogeneous.

No deviation from the baseline is observed in the GP trace, confirming the qualitative observation from the GP pseudo-image. This fact implies alignment of the lipid molecules along the bilayer normal in these domains. The average intensity of the green channel pseudo-image is approximately four counts per pixel, while the intensity found for the dark spots is approximately two counts per pixel. The size of these first-forming domains is on the order of 1–2 μm and their time of permanence on the circular trajectory is on the order of 0.1–1 s. In the first stages of phase separation we typically observe one domain per scanned orbit. The 2D histograms calculated at this temperature (Fig. 4 *C*) are very similar to those calculated at temperatures above the phase separation. A short tail stretching toward low intensity values is, however, visible.

After ~2 min at 41.0 ± 0.5°C (Fig. 4, *bottom panel*) we observe an increase in the size of the domains crossing the scanned orbit. At this time we also observe the coexistence of 1–2 μm domains described above with larger (4–6 μm in size) domains that remain on the orbit for 5–10 seconds (Fig. 4 *E*). In these domains the intensity drops to less than an average of one count per pixel in both channels and the GP reaches gel-like values. We see that the GP of the first-forming domains increases with time while the general shape of the domains remains unchanged at this stage (data not shown). At this time we observe a dramatic change in the shape of both GP versus I_{440} and I_{490} histograms (Fig. 4 *F*) as both distributions are not confined to a defined region in the GP/intensity plane, but stretch toward the low intensities and high GP region compatible with the presence of gel domains. The white curve in the 2D histograms in Fig. 4 *F* represents the two-state approximation curve calculated for these data. The GP-autocorrelation function calculated from the data at this time (Fig. 4 *G*) shows an increase in the $G(0)$ due to the increase in contrast between the domains and the liquid-crystalline background.

As explained in Methods, we used the parameters describing the two-state approximation curves in Fig. 4 *F* to

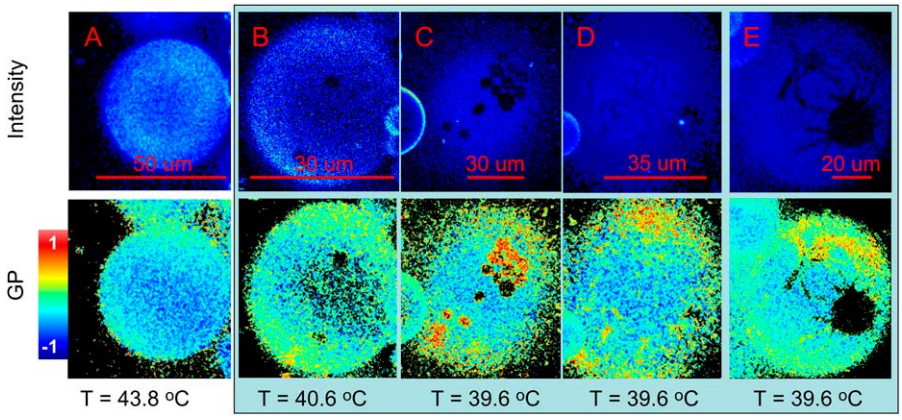

FIGURE 3 Time evolution of domain morphology at $T = 40 \pm 1$°C. (*Top panel*) Green channel fluorescence intensity; (*bottom panel*) GP image. (*A*) Polar region of a GUV before phase separation; (*B*) onset of phase separation as detected by imaging; (*C*) domain coalescence at $t = 10$ min; (*D*) wire-shaped domains at $t = 34$ min; and (*E*) domains at equilibrium at $t > 55$ min.

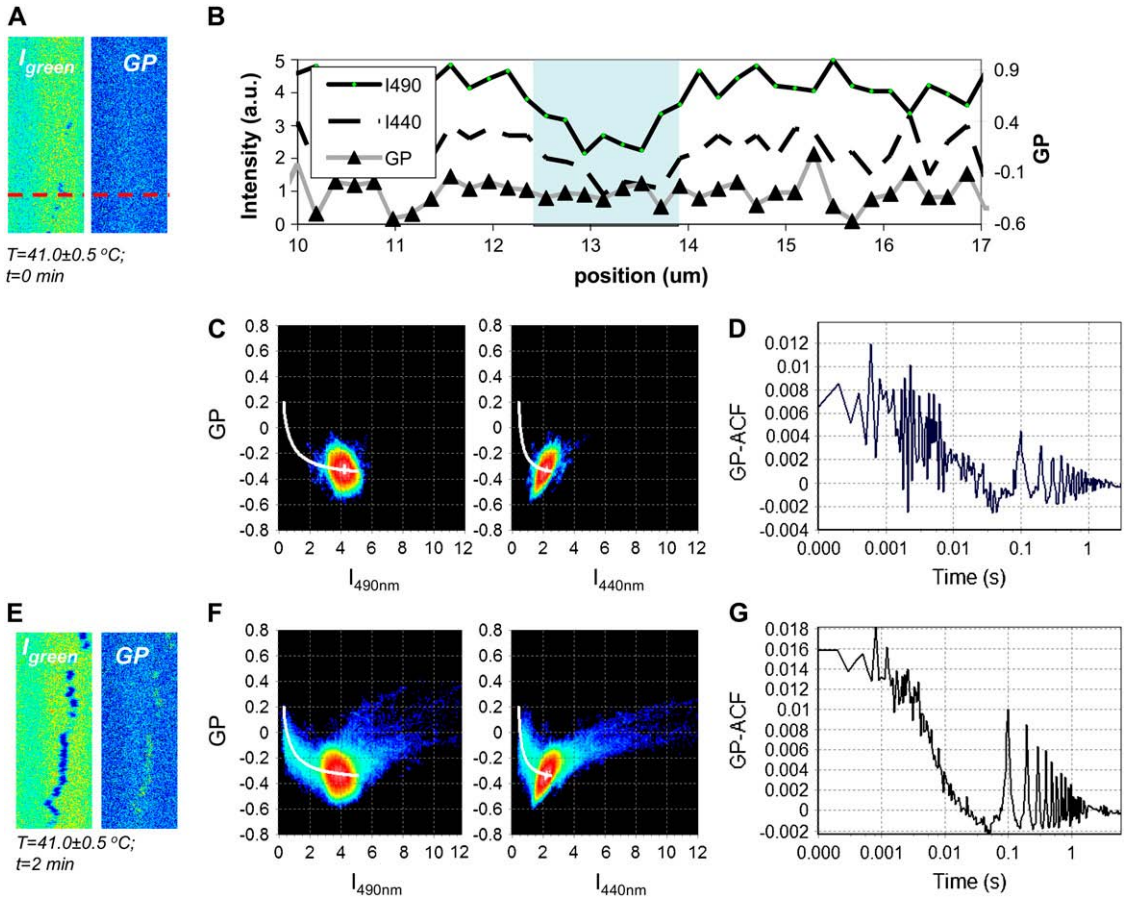

FIGURE 4 Onset of phase separation-circular scanning data for DPPC/DLPC 1:1 at 40 ± 1°C. Onset of phase separation, $t = 0$ min (*top panel*) and $t = 2$ min (*bottom panel*). (*A* and *E*) Pseudo-images of intensity in the green channel (*left*) and GP (*right*), (*C* and *F*) 2D histogram of GP versus intensity in the green channel, I_{490} (*left*) and 2D histogram of GP versus intensity in the blue channel, I_{440} (*right*). (*D* and *G*) GP autocorrelation curve. In panel *B*, the intensity (I_{490}, *solid line*; I_{440}, *dashed line*) and GP (*triangles*) traces for the red dashed line in the pseudo-images (*bottom part* of *A*) show that while we observe a dip in the intensity traces (*highlighted area* on the *plot*) corresponding to the domain, no deviation from the baseline of −0.34 is present in the GP trace. For both top and bottom panels $t_p = 0.1$ s, $n_p = 1000$, and $d_p = 21$ nm. The 20.8 mm portion of the scanned trajectory in a 25.6s time frame.

calculate the gel fraction corresponding to each GP and intensity value. We therefore proceeded to map areas of a given gel fraction back into the pseudo-image. The result of this analysis for the data at the onset of phase separation is shown in Fig. 5. The analysis of the data acquired at 41.0 ± 0.5°C allows us to follow the evolution of gel domains in the first stages of phase separation. In Fig. 5 *B*, areas with a gel fraction α (see Eq. 3) between 32% and 52% are highlighted in red. The white arrows in the figures indicate when the first micron-sized domains with these gel fractions are observed. We calculated the average size of these domains to be on the order of 1.5 μm, well above our system PSF. In Fig. 5, *C* and *D*, areas with $52\% < \alpha < 73\%$ and $88\% < \alpha < 94\%$, respectively, are shown. We find extended domains with a gel fraction >90% (*white arrow* in Fig. 5 *D*) after ~5 min from the onset of phase separation.

Fig. 6 shows the circular scanning data acquired after 15 min from the onset of phase separation, in a temperature range of 40 ± 1°C. At time $t = 15$ min (Fig. 6 *A*), we observe a higher number of domains crossing the scanned orbit. Both the intensity and GP traces rendered in pseudo-images (*left side* of Fig. 6 *A*) show the presence of gel-like domains (as detected by low intensity and high GP) that remain in the circular trajectory for 10–15 s. We also observe changes in the morphology of the smaller domains from round and compact to weblike. The skewed trajectory of the domains on the pseudo-image and the decrease in the time of permanence of the smaller domains on the trajectory reveals an increase in motility of the domains on the GUV membrane. At $t = 22$ min (pseudo-images in *left side* of Fig. 6 *B*) we observe that the domains are no longer isolated, but are more interconnected with each other. They are also larger and more stable. In addition, the pseudo-images reveal the presence of numerous regions with intermediate values of GP and intensity. At $t = 44$ min, we start observing a decrease in the number of domains per scanned orbit, and a decrease in their motility as shown by the pseudo-images at the left of Fig. 6 *C* in which we can see a large domain persisting in the same position for

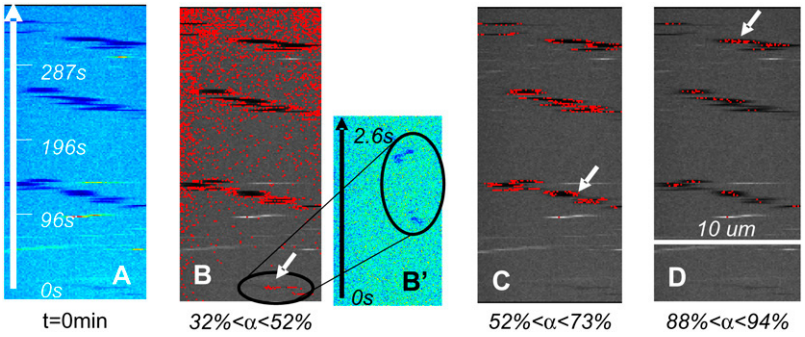

FIGURE 5 Gel phase percentage at different times for DPPC/DLPC 1:1. (*A*) Green channel intensity pseudo-image at $t = 0$ and $T = 41.0 \pm 0.5$°C. The image is calculated by binning the points by 5 and averaging the orbits by 15. (*B–D*) Location of the pixels with a given gel fraction on the pseudo-image. The white arrows indicate the first occurrence in time of a domain >1 μm with the gel fraction specified on the bottom of each image. The letter α indicates the gel fraction as defined in Eq. 3. Panel *B′* shows the zoom-in of the highlighted region in panel *B*.

the whole time of the image (25.6 s). The same type of behavior is observed in all the data acquired after 45 min from the onset of phase separation. The central parts of Fig. 6, *A–C*, show the 2D histograms relative to the data rendered in the corresponding pseudo-images. We observe that the 2D distribution of the data acquired at these times is well approximated by the two-state curve.

While the pseudo-images allow visualizing selected portions of the intensity and GP traces, by calculating the GP-autocorrelation functions for these files, we can estimate the changes in the average size, density, and stability of the GP domains at different times after phase separation (Fig. 6 *A–C*, *right sides*). From these curves we observe an increase in the $G(0)$ with time which is related to the decrease in the number of domains crossing the trajectory. Also, at later times we observe a slower decay in the first portion of the GP-autocorrelation curve, indicating a larger average size of the gel domains. The decrease in domain motility after the

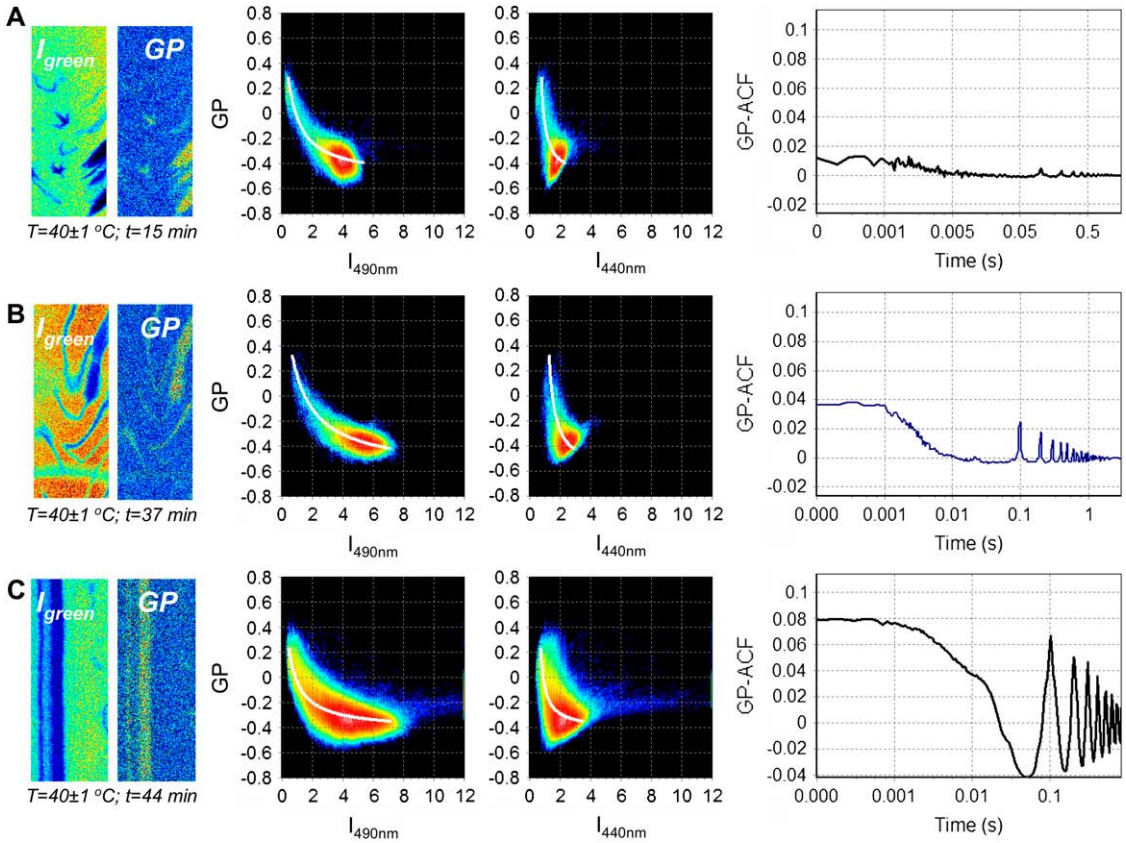

FIGURE 6 Lipid domain evolution-circular scanning data at 40 ± 1°C for DPPC/DLPC 1:1. (From *left* to *right*) Pseudo-images of intensity in the green channel and GP, 2D histogram of GP versus intensity in the green channel (I_{490}), and 2D histogram of GP versus intensity in the blue channel (I_{440}), GP autocorrelation curve. The white line in each of the 2D distributions represents the two-state approximation curve calculated from Eq. 4. (*A*) $t = 15$ min, $n_p = 2000$, and $d_p = 21$ nm; (*B*) $t = 37$ min, $n_p = 1000$, and $d_p = 28$ nm; (*C*) $t = 44$ min, $n_p = 1000$, and dp $= 28$ nm. Each pseudo-image shows a 20.8-μm portion of the scanned trajectory in a 25.6-s time frame.

first 20 min from phase separation determines the slower decay of the overall GP-autocorrelation curves from data acquired at later times.

We used the 2D histograms to map areas of 50% or less gel fraction back into the pseudo-images at times between 15 and 75 min. The results of this procedure are summarized in Fig. 7. The figure shows that areas of several microns (up to 5 μm at $t = 15$ min and $\sim$10 μm at $t = 22$ min) with $\alpha < 50\%$ are observed up to 22 min after the onset of phase separation. After $\sim$1 h ($t = 75$ min), however, such areas disappear and we find $\alpha < 50\%$ only at the borders of larger domains.

Data acquired after 50 min from the onset of phase separation display a deviation of the 2D distributions from the two-state model as can be seen from Fig. 8 (*B–F*, *bottom panels*). A deviation of the 2D histograms from the non-interacting two-state approximation model (see Methods) suggests interaction between the two lipid phases. We can investigate how the two lipids species influence each other by mapping on the pseudo-images the areas of the 2D histogram that deviate from the two-state model curve. This is shown in Fig. 8. We can isolate the areas of the pseudo-image that lie on the two-state curve from those that deviate from it. We refer to regions 1 and 2 in Fig. 8 *A*. The high GP domain in region 1 is the only one with a gel fraction >90% in this image. The size of this domain is $\sim$2 μm. It lies entirely on the two-state curve, is surrounded by a liquid-crystal region and it is isolated from other domains. On the contrary, no significant portion of region 2 is found to lie on the two-state curve. The domain in region 2 is composed of a central region with liquid-crystalline-like GP and low intensity and of a peripheral region with low intensity and intermediate GP. Note that these two subregions correspond to two different areas of the 2D distribution.

DISCUSSION

The data presented above were collected with the purpose of detecting and investigating lipid phase fluctuations on the micron-submicron scale in lipid bilayers. Phase fluctuations were induced on a membrane composed of a binary mixture displaying phase separation (DLPC/DPPC 1:1) by lowering the temperature to the main phase transition temperature of DPPC.

Data at temperatures above phase separation

Although we observe clear evidence of phase separation in the fluorescence pseudo-images in both channels only at 41.0 $\pm$ 0.5°C, the circular scanning data collected at temperature above phase separation suggest the presence of heterogeneity also in the liquid crystalline phase (Fig. 2). The GP-autocorrelation curves at 45.6°C (data not shown) and 43.1°C show correlation for the first 60 data points corresponding to a spatial and temporal length of 1.2 μm (greater than the spatial resolution of the microscope) and 6 ms, respectively, which implies the presence of long-range organization of lipid membrane at this temperature. However, we do not observe any domains larger than the PSF size in either intensity or GP traces at this temperature. One possible explanation for these observations is the presence of subdiffraction lipid domains at this temperature that then coalesce to form micron-size domains after the phase separation temperature is reached. When phase separation occurs we observe an increase in the amplitude of the GP-autocorrelation curves and a broadening of the peaks. A larger value of the $G(0)$ indicates fewer domains and the broadening of the peaks indicates a larger size of the domains.

Data at the phase separation temperature

From the images in Fig. 3, the domains always appear to be dark and with high GP. This implies that the two leaflets of the GUV membrane are aligned (orthogonally to the plane of the membrane), i.e., the gel domains are not confined to only one leaflet, but they span the bilayer. This observation is in agreement with many experiments on lipid mixtures utilizing different types of dyes (for example, (15,17,25)). The following analysis of the circular scanning data is geared toward the understanding of the dynamics of leaflets coupling.

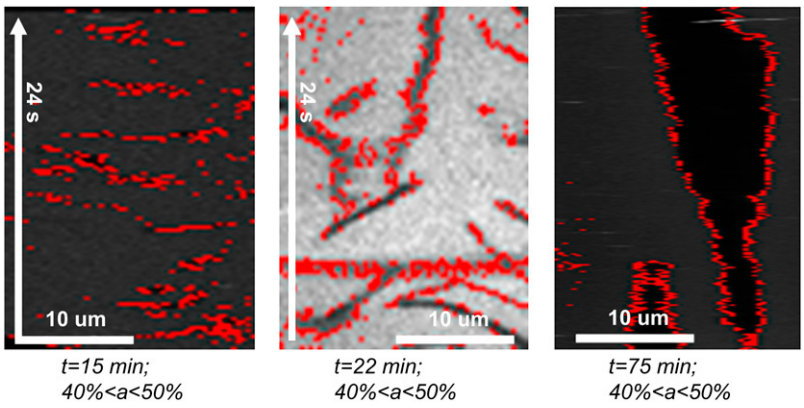

FIGURE 7 Evolution of 50% gel fraction domains in DPPC/DLPC 1:1. In the three panels the areas with 50% gel fraction are highlighted in red. At $t = 15$ min these domains have a size on the order of 2–5 μm and remain on the trajectory for $\sim$1 s. At $t = 22$ min we observe large 50% gel fraction domains spanning almost the entire trajectory in addition to smaller ones. At $t = 75$ min, regions with $\alpha < 50\%$ are observed only at the borders of larger stable domains. A white bar in each figure indicates the dimension of the domains. The letter α indicates the gel fraction as defined in Eq. 3.

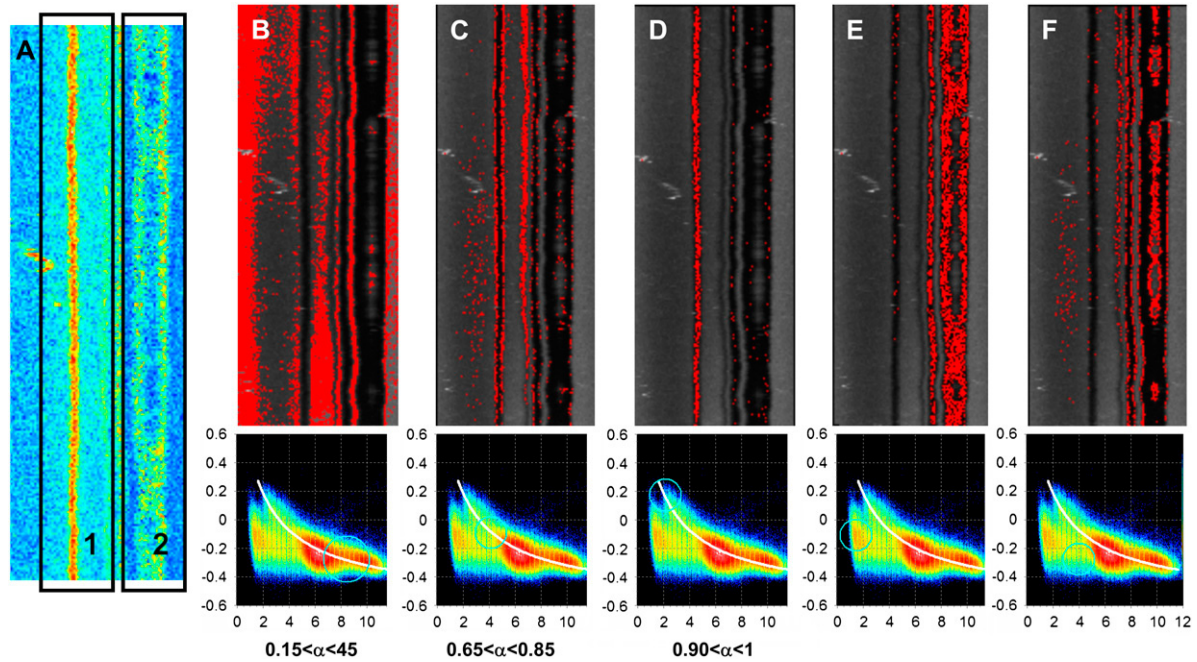

FIGURE 8 Interaction of the two lipid species on the phase behavior of each other for DPPC/DLPC 1:1: (*A*) GP pseudo-image of data acquired at $T = 40 \pm 1°C$ and $t = 75$ min. Points in a given range on GP and intensity (represented by the *cyan circle* in the 2D histogram) are highlighted in red on the black and white pseudo-images. (*B–D*) Areas with different gel fraction that follow on the two-state curve. The cyan circles in the 2D histograms at the bottom of each pseudo-image show the portion of 2D distribution that corresponds to the highlighted points in the pseudo-images. (*E*) Points outside the two-state curve with low intensity and intermediate GP. (*F*) Points outside the two-state curve with low intensity and low GP.

Several theoretical and experimental works have identified in the acyl-chains' excluded volume interactions, the main interaction leading to the lipid density phase transition. This transition is cooperative in nature due to the fact that all the molecules in a certain area need to rearrange to accommodate the changes in excluded volume (50). If we consider only the change in surface density of the lipid molecules, we see that the two leaflets do not need to be connected. However, the increase in lipid density is accompanied by the thickening of the bilayer. In the binary mixture case it has been proposed that the longer chain lipid penetrates the other layer, inducing the coupling between the two leaflets of the bilayer.

The fact that the first 1–2-μm-sized domain we were able to resolve appear only in the intensity trace and not in the GP trace implies that the molecules forming these domains are highly radially aligned. Here we exploited the correlation between molecular alignment (low intensity) and high GP to estimate the portion of lipid molecules in the gel phase in one pixel assuming a two-state scenario. To address the issue of leaflet coupling, we selected those pixels with values of intensity and GP that are consistent with a fraction of molecules in the gel phase $\leq$50%. Only this region can be consistent with a scenario in which the two leaflets are not yet coupled.

We estimated that the gel fraction of the first forming domains (Figs. 4 *A* and 5 *B*) is <50%. A gel fraction of 50% implies that half the molecules in a pixel are in the gel phase, but per se it is not sufficient to determine whether these molecules are confined to only one of the leaflets. However, if we think about these two scenarios at the molecular level, we have that in the noncoupling case the surface area occupied by the ordered domain will have twice the extension of that of leaflet-coupled microdomains. In our experiments, the domains with $\alpha < 50\%$ are larger than the PSF. In the case of submicron domains spanning the bilayer, we would have to assume that these domains were not interconnected. If this was the case, however, we would expect to detect also smaller domains <0.7 μm in size) with $\alpha < 50\%$, while the only observed domains with $40\% < \alpha < 50\%$ are well localized in micron-size structures. Moreover, in data acquired 15 min after the onset of phase separation we observe 5-μm-large domains with $\alpha < 50\%$, and at $t = 22$ min we detect 10-μm-large domains with $\alpha < 50\%$. We therefore conclude that domains confined to only one leaflet exist in the initial stages of phase separation for this lipid mixture up to ~20 min from the onset of phase separation. The data presented in Fig. 5 show that coupling of the leaflets is already present 2 min after the detection of the first domain and that it is completed after 5 min, when we detect extended areas with $\alpha > 90\%$. After 50 min from the onset of phase separation, the areas with $\alpha <$ 50% are confined only to the borders of larger stable domains. We expect this type of behavior to be a consequence of the packing ''defects'' at the liquid-gel interface.

The 2D histogram also yields information on the influence of the two coexisting lipid species on each other properties.

The data presented above show very little deviation from a two-state model with no interaction between the two phases for the first hour after the onset of phase separation. This implies that, in the first stages of phase separation the two lipid phases do not interact significantly with each other at least on the micron-length-scale considered here. After 1 h from the onset of phase separation, however, the 2D distribution drastically deviates from the two-state curve indicating the interaction between the two lipid phases (27). At this time, the domains are large, stable (Fig. 9), and occupy a large portion of the membrane. The mapping of the 2D histogram to the pseudo-image discussed above, allows us to relate the deviation from the two-state model with the local topology of the domain. In the case presented in Fig. 8 we show how a large gel domain induces radial alignment on a low GP region. The low GP value found in this area implies that water is present at the glycerol backbone of the lipids, thus implying that the lipids are loosely packed. At the same time the low intensity in both channels implies that the lipid acyl chains are aligned along the membrane normal. It is reasonable to assume that the low GP region embedded in the high GP domain in region 2 of Fig. 8 *A* is rich in DLPC while the high GP region is rich in DPPC as a result of domain coalescence. This scenario is particularly interesting in relation to the problem of leaflet coupling. In fact, one of the possible explanations of this effect is that the longer DPPC molecules are penetrating in the opposite leaflet and inducing alignment in the DLPC molecules.

Another aspect of domain formation which can be deduced from our data is the correlation between domain size, morphology, and motion. In Fig. 9 we plotted the fraction of gel domains with $\alpha > 40\%$ versus time and we indicated the time window in which domain motion is observed. We notice that motion is observed when a total gel fraction of 10% is reached and it stops when the curve reaches a plateau.

For the first 20 min after the onset of phase separation, we observe round domains of size ranging from 3 to 9 μm diffusing on the GUV membrane with directional motion. We do not observe round domains larger than 9 μm. Phase separation proceeds by branching out of weblike domains. Larger domains appear to be generated by coalescence of smaller domains. From the circular scanning data we see that the first domains to form are stable on the circular trajectory (although directional motion is observed which seems to proceed in jumps). The domain in Fig. 4 *E* maintains the same position on the orbit for at least 6 s. As the number of domains increases (from both the imaging and circular scanning data) we observe a faster domain motion (Fig. 6, *A* and *B*). As the domains coalesce and increase in size, their motion slows down and eventually stops after 1 h (Fig. 6 *C* and Fig. 8).

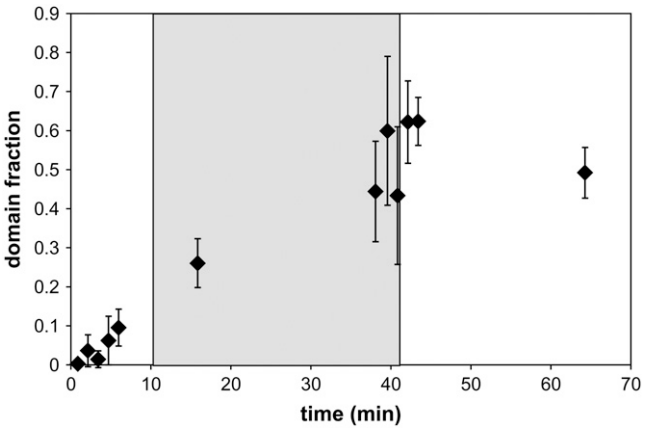

FIGURE 9 Domain motion and domain formation. The domain fraction was calculated as the ratio of the number of pixels with a gel fraction >40% to the total number of pixels per pseudo-image, and plotted as a function of time. The shaded area highlighted in the figure shows the time interval where domain motion is observed.

CONCLUSION

In this work we used a combination of imaging and fluctuations techniques and data analysis to investigate spatial and temporal fluctuations in lipid organization at different stages of lipid phase separation in a binary mixture. Our data show high heterogeneity in the lipid organization at temperatures above and below phase separation. The methodology presented above allowed studying the temporal evolution of gel phase domains at the onset of phase separation as well as the correlation between domain topology and lipid ordering locally.

The data acquired before phase separation suggest fluctuations in the lipid organization with a lifetime shorter than 0.1 s and a characteristic length of 1.2 μm.

In the discussion above we were able to show that coupling between the two leaflets of the bilayer occurs in the first 5 min from the onset of phase separation and that domains confined to only one leaflet exist for the first 22 min from the onset of phase separation. Our analysis indicate that for the first 45–50 min from the onset of phase separation the two lipid phases do not strongly influence the phase behavior of each other on the micron-length scale. However, data acquired after 50 min show deviation from the two-state model which appears to be correlated with the domain morphology.

Another interesting result of this study is the fact that domain formation appears correlated to domain motion. The speed of the domain motion on the GUV surface appears to be related to the number and size of the domains.

From the results presented it is clear that even without the introduction of further complexities, such as proteins, sterols, and other types of lipids, simple model membrane systems composed of at least two different lipids have the capability of sustaining stable structural heterogeneities. It may very well be that the introduction of additional varieties of lipids and sterols serve mainly to enforce and modulate this inherent tendency.

The methods developed in this work to address the above questions could also be used to investigate more biologically relevant samples such as the surfaces of cells. The technique is relatively noninvasive, only requiring the co-mingling of Laurdan with the system of observation.

Dr. Sabrina Beretta died of cancer at the time that this article was ready to be submitted. Dr. Beretta performed many of the measurements in this work. We dedicate this article to her memory.

We thank Dr. Susana Sanchez for the insightful discussion and suggestions.

The experiments presented were carried out at the Laboratory for Fluorescence Dynamics with the financial support of the National Institute of Health grant (No. P41-03155).

REFERENCES

1. Brown, D. A., and E. London. 2000. Structure and function of sphingolipid- and cholesterol-rich membrane rafts. *J. Biol. Chem.* 275:17221–17224.
2. Jacobson, K., and C. Dietrich. 1999. Looking at lipid rafts? *Trends Cell Biol.* 9:87–91.
3. Ono, A., and E. O. Freed. 2001. Plasma membrane rafts play a critical role in HIV-1 assembly and release. *Proc. Natl. Acad. Sci. USA.* 98:13925–13930.
4. Liao, Z., D. R. Graham, and J. E. Hildreth. 2003. Lipid rafts and HIV pathogenesis: virion-associated cholesterol is required for fusion and infection of susceptible cells. *AIDS Res. Hum. Retroviruses.* 19:675–687.
5. Mayor, S., and M. Rao. 2004. Rafts: scale-dependent, active lipid organization at the cell surface. *Traffic.* 5:231–240.
6. Gri, G., B. Molon, S. Manes, T. Pozzan, and A. Viola. 2004. The inner side of T cell lipid rafts. *Immunol. Lett.* 94:247–252.
7. Kusumi, A., I. Koyama-Honda, and K. Suzuki. 2004. Molecular dynamics and interactions for creation of stimulation-induced stabilized rafts from small unstable steady-state rafts. *Traffic.* 5:213–230.
8. Arnold, A., M. Paris, and M. Auger. 2004. Anomalous diffusion in a gel-fluid lipid environment: a combined solid-state NMR and obstructed random-walk perspective. *Biophys. J.* 87:2456–2469.
9. Veatch, S. L., I. V. Polozov, K. Gawrisch, and S. L. Keller. 2004. Liquid domains in vesicles investigated by NMR and fluorescence microscopy. *Biophys. J.* 86:2910–2922.
10. Tokumasu, F., A. J. Jin, G. W. Feigenson, and J. A. Dvorak. 2003. Atomic force microscopy of nanometric liposome adsorption and nanoscopic membrane domain formation. *Ultramicroscopy.* 97:217–227.
11. Ratto, T. V., and M. L. Longo. 2002. Obstructed diffusion in phase-separated supported lipid bilayers: a combined atomic force microscopy and fluorescence recovery after photobleaching approach. *Biophys. J.* 83:3380–3392.
12. Bagatolli, L. A. 2003. Direct observation of lipid domains in free standing bilayers: from simple to complex lipid mixtures. *Chem. Phys. Lipids.* 122:137–145.
13. Bagatolli, L., and E. Gratton. 2000. Two-photon fluorescence microscopy of coexisting lipid domains in giant unilamellar vesicles of binary phospholipid mixtures. *Biophys. J.* 78:434–447.
14. Bagatolli, L. A., S. A. Sanchez, T. Hazlett, and E. Gratton. 2003. Giant vesicles, Laurdan, and two-photon fluorescence microscopy: evidence of lipid lateral separation in bilayers. *Methods Enzymol.* 360:481–500.
15. Korlach, J., P. Schwille, W. W. Webb, and G. W. Feigenson. 1999. Characterization of lipid bilayer phases by confocal microscopy and fluorescence correlation spectroscopy. *Proc. Natl. Acad. Sci. USA.* 96: 8461–8466.
16. Baumgart, T., S. T. Hess, and W. W. Webb. 2003. Imaging coexisting fluid domains in biomembrane models coupling curvature and line tension. *Nature.* 425:821–824.
17. Kahya, N., D. Scherfeld, K. Bacia, and P. Schwille. 2004. Lipid domain formation and dynamics in giant unilamellar vesicles explored by fluorescence correlation spectroscopy. *J. Struct. Biol.* 147: 77–89.
18. Veatch, S. L., and S. L. Keller. 2003. Separation of liquid phases in giant vesicles of ternary mixtures of phospholipids and cholesterol. *Biophys. J.* 85:3074–3083.
19. Hac, A. E., H. M. Seeger, M. Fidorra, and T. Heimburg. 2005. Diffusion in two-component lipid membranes—a fluorescence correlation spectroscopy and Monte Carlo simulation study. *Biophys. J.* 88:317–333.
20. Laradji, M., and P. B. Kumar. 2006. Anomalously slow domain growth in fluid membranes with asymmetric transbilayer lipid distribution. *Phys. Rev. E Stat. Nonlin. Soft Matter Phys.* 73:040901.
21. Michonova-Alexova, E. I., and I. P. Sugar. 2002. Component and state separation in DMPC/DSPC lipid bilayers: a Monte Carlo simulation study. *Biophys. J.* 83:1820–1833.
22. Arcaro, A., C. Gregoire, T. R. Bakker, L. Baldi, M. Jordan, L. Goffin, N. Boucheron, F. Wurm, P. A. van der Merwe, B. Malissen, and I. F. Luescher. 2001. CD8β endows CD8 with efficient coreceptor function by coupling T cell receptor/CD3 to raft-associated CD8/p56(lck) complexes. *J. Exp. Med.* 194:1485–1495.
23. Bretscher, M. S. 1972. Asymmetrical lipid bilayer structure for biological membranes. *Nat. New Biol.* 236:11–12.
24. Kiessling, V., J. M. Crane, and L. K. Tamm. 2006. Transbilayer effects of raft-like lipid domains in asymmetric planar bilayers measured by single molecule tracking. *Biophys. J.* 91:3313–3326.
25. Bagatolli, L., and E. Gratton. 2000. A correlation between lipid domain shape and binary mixture composition in free standing bilayers: a two-photon fluorescence microscopy study. *Biophys. J.* 79:434–447.
26. Almeida, P. F., W. L. Vaz, and T. E. Thompson. 1992. Lateral diffusion and percolation in two-phase, two-component lipid bilayers. Topology of the solid-phase domains in-plane and across the lipid bilayer. *Biochemistry.* 31:7198–7210.
27. Parasassi, T., G. De Stasio, A. d'Ubaldo, and E. Gratton. 1990. Phase fluctuation in phospholipid membranes revealed by Laurdan fluorescence. *Biophys. J.* 57:1179–1186.
28. Bagatolli, L. A., T. Parasassi, and E. Gratton. 2000. Giant phospholipid vesicles: comparison among the whole lipid sample characteristics using different preparation methods: a two photon fluorescence microscopy study. *Chem. Phys. Lipids.* 105:135–147.
29. Stottrup, B. L., S. L. Veatch, and S. L. Keller. 2004. Nonequilibrium behavior in supported lipid membranes containing cholesterol. *Biophys. J.* 86:2942–2950.
30. Jorgensen, K., M. M. Sperotto, O. G. Mouritsen, J. H. Ipsen, and M. J. Zuckermann. 1993. Phase equilibria and local structure in binary lipid bilayers. *Biochim. Biophys. Acta.* 1152:135–145.
31. Winter, R., A. Gabke, C. Czeslik, and P. Pfeifer. 1999. Power-law fluctuations in phase-separated lipid membranes. *Phys. Rev. E Stat. Phys. Plasmas Fluids Relat. Interdiscip. Topics.* 60:7354–7359.
32. Bagatolli, L., E. Gratton, and G. Fidelio. 1998. Water dynamics in glycosphingolipids aggregates studied by Laurdan fluorescence. *Biophys. J.* 75:331–341.
33. Bagatolli, L. A., T. Parasassi, G. D. Fidelio, and E. Gratton. 1999. A model for the interaction of 6-lauroyl-2-(*n*,*n*-dimethylamino)naphthalene with lipid environments: implications for spectral properties. *Photochem. Photobiol.* 70:557–564.
34. Parasassi, T., G. De Stasio, A. d'Ubaldo, and E. Gratton. 1991. Quantization of lipids phases in phospholipids vesicles by the generalized polarization of Laurdan fluorescence. *Biophys. J.* 60: 179–189.
35. Parasassi, T., G. Ravagnan, R. Rusch, and E. Gratton. 1993. Modulation and dynamics of phase properties in phospholipid mixtures detected by Laurdan fluorescence. *Biochem. Photobiol.* 57:403–410.
36. Parasassi, T., and E. Gratton. 1995. Membrane lipid domains and dynamics as detected by Laurdan fluorescence. *J. Fluor.* 5:59–69.

37. Parasassi, T., E. Gratton, W. M. Yu, P. Wilson, and M. Levi. 1997. Two-photon fluorescence microscopy of Laurdan generalized polarization domains in model and natural membranes. *Biophys. J.* 72:2413–2429.

38. Angelova, M. I., and D. S. Dimitrov. 1986. Liposome electroformation. *Faraday Discuss. Chem. Soc.* 81:303–311.

39. Bagatolli, L. A., and E. Gratton. 1999. Two-photon fluorescence microscopy observation of shape changes at the phase transition in phospholipid giant unilamellar vesicles. *Biophys. J.* 77:2090–2101.

40. Macgregor, R. B., and G. Weber. 1981. Fluorophores in polar media: spectral effects of the Langevin distribution of electrostatic interactions. *Ann. N. Y. Acad. Sci.* 366:140–150.

41. Weber, G., and F. J. Farris. 1979. Synthesis and spectral properties of a hydrophobic fluorescent probe: 2-dimethylamino-6-propionylnaphthalene. *Biochemistry.* 18:3075–3078.

42. Parasassi, T., F. Conti, and E. Gratton. 1986. Fluorophores in a polar medium: time dependence of emission spectra detected by multifrequency phase and modulation fluorometry. *Cell. Mol. Biol.* 32: 99–102.

43. Parasassi, T., F. Conti, and E. Gratton. 1986. Time-resolved fluorescence emission spectra of Laurdan in phospholipid vesicles by multifrequency phase and modulation fluorometry. *Cell. Mol. Biol.* 32: 103–108.

44. Parasassi, T., E. Krasnowska, and L. Bagatolli. 1998. Laurdan and Prodan as polarity-sensitive fluorescent membrane probes. *J. Fluor.* 8:365–373.

45. Krasnowska, E. K., E. Gratton, and T. Parasassi. 1998. Prodan as a membrane surface fluorescence probe: partitioning between water and phospholipid phases. *Biophys. J.* 74:1984–1993.

46. Berland, K. M., P. T. So, and E. Gratton. 1995. Two-photon fluorescence correlation spectroscopy: method and application to the intracellular environment. *Biophys. J.* 68:694–701.

47. Berland, K. M., P. T. So, Y. Chen, W. W. Mantulin, and E. Gratton. 1996. Scanning two-photon fluctuation correlation spectroscopy: particle counting measurements for detection of molecular aggregation. *Biophys. J.* 71:410–420.

48. Digman, M. A., C. M. Brown, P. Sengupta, P. W. Wiseman, A. R. Horwitz, and E. Gratton. 2005. Measuring fast dynamics in solutions and cells with a laser scanning microscope. *Biophys. J.* 89:1317–1327.

49. Digman, M. A., P. Sengupta, P. W. Wiseman, C. M. Brown, A. R. Horwitz, and E. Gratton. 2005. Fluctuation correlation spectroscopy with a laser-scanning microscope: exploiting the hidden time structure. *Biophys. J.* 88:L33–L36.

50. Nagle, J. F. 1980. Theory of the main lipid bilayer phase transition. *Annu. Rev. Phys. Chem.* 31:157–195.